BIBECHANA
Vol. 23, No. 3, August 2026, 173–188

ISSN 2091-0762 (Print), 2382-5340 (Online)
Journal homepage: http://nepjol.info/index.php/BIBECHANA
Publisher: Dept. of Phys., Mahendra Morang A. M. Campus (Tribhuvan University), Biratnagar

First-principles investigation of structural, elastic, electronic, and optical properties of Mg_3BaO_4 and Sr_3CdO_4 for optoelectronic applications

Uchit Chaudhary[1,2], Subash Dahal[1*], Gopi Chandra Kaphle[2], Shashit Kumar Yadav[1*]

[1]*Department of Physics, Mahendra Morang Adarsh Multiple Campus, Tribhuvan University, Biratnagar 56613, Nepal.*
[2]*Central Department of Physics, Tribhuvan University, Kirtipur 44613, Kathmandu, Nepal.*

*Corresponding authors: Email: sashit.yadav@mmamc.tu.edu.np; subashdahal15@gmail.com

Abstract

This study presents a comprehensive first-principles investigation of the structural, elastic, electronic, and optical properties of Mg_3BaO_4 and Sr_3CdO_4 compounds, emphasizing their potential for optoelectronic applications. These compounds are found to be thermodynamically and mechanically stable. The electronic band structures, analyzed using the TB-mBJ method, revealed direct band gap of 2.29 eV and indirect band gap of 2.64 eV for Mg_3BaO_4 and Sr_3CdO_4, respectively. Furthermore, their optical properties, including dielectric functions, absorption coefficients, and refractive indices, indicated strong absorption in the UV region, highlighting their suitability for high-performance solar cells, optical sensors, and light-emitting devices. These findings provide critical insights into the optoelectronic potential of Mg_3BaO_4 and Sr_3CdO_4, paving the way for experimental validation and practical applications.

Keywords
First-principles, optoelectronic, solar cells, optical sensors, light-emitting devices.

Article information
Manuscript received: June 10, 2026; Revised: August 22, 2026; Accepted: August 28, 2026
DOI https://doi.org/10.3126/bibechana.v23i3.100227

1 Introduction

Metal oxides represent a crucial and versatile class of materials with extensive applications across a broad range of industries. Over the decades, their study has driven significant advancements in diverse fields, including magnetism, semiconductors, optoelectronics, catalysis, thermoelectric devices, and energy storage [1–9]. Through detailed investigations of various metal oxide families such as binary metal oxides, transition metal oxides, perovskites, and spinel oxides, researchers have developed a comprehensive understanding of their unique properties and vast potential applications.

For example, zinc oxide (ZnO) has emerged as a key material in optoelectronic devices and gas sensors due to its favorable electronic properties [10]. Nickel oxide (NiO), on the other hand, is widely utilized in electrochemical applications and as a catalyst in oxidation reactions [11]. Titanium dioxide (TiO_2) is another well-studied material, particularly for its photocatalytic properties, which hold great promise for environmental cleanup and energy conversion applications [12]. Similarly, manganese oxide (MnO_2) is crucial in battery technologies and catalysis [13]. Meanwhile, vanadium dioxide (VO_2) is extensively researched for its metal-insulator transition, making it a strong candidate for smart windows and advanced electronic devices [14]. Tin oxide (SnO_2) is noted for its electronic structure and optical properties, which enhance its utility in catalysis, sensors, and optoelectronics [15]. Additionally, iron oxides, particularly magnetite (Fe_3O_4) and hematite (α-Fe_2O_3), have gained attention for their magnetic properties and effectiveness in environmental remediation [16]. Chromium oxide (Cr_2O_3) and neodymium oxide (Nd_2O_3) are recognized for their exceptional high-temperature stability, making them ideal for protective coatings [17].

Further, $PdAlO_2$, $PdCrO_2$, and $PdRhO_2$, with their indirect band gaps ranging from 2.14 to 2.68 eV, show great promise for optoelectronic and photovoltaic applications due to their favorable thermoelectric properties, such as low thermal conductivity, high Seebeck coefficients, and enhanced performance at elevated temperatures [18]. Wide band gap semiconductors like zinc aluminate ($ZnAl_2O_4$), zinc gallate ($ZnGa_2O_4$), and zinc indium oxide ($ZnIn_2O_4$) also show potential in photoelectronics and optics [19]. The investigation of spinel oxides, including $GeMg_2O_4$, $GeZn_2O_4$, and $GeCd_2O_4$, demonstrates that the band gaps of these compounds decrease as the atomic size of the constituent elements (Mg, Zn, and Cd) increases, confirming that these compounds are direct-band-gap materials [20]. First-principles calculations on $ZnFe_2O_4$ reveal its mechanical stability, direct bandgap semiconducting nature, pressure-dependent bandgap, and stronger Zn–O bonds compared to Fe–O, with optical properties aligning with experimental data [21].

A thermodynamically stable cubic phase, Mg_3ZnO_4 ($Pm\bar{3}m$), has been discovered, exhibiting mechanical and dynamic stability, with an indirect band gap of ($\sim$ 5.95 eV) [22]. Mg_3CdO_4 is a semiconductor with an indirect band gap of 5.19 eV, and its detailed optical property analysis, including dielectric function, refractive index, absorption coefficient, reflectivity, and loss function, highlights its potential for optoelectronic applications [23]. The study of XBe_3O_4 (X = Li, Na, K) compounds demonstrated that these materials are energetically stable in their ferromagnetic phase, with some of them exhibiting mechanical stability, ductility, and anisotropy, making promising candidates for spintronic applications due to their high Curie temperatures [24]. Theoretical studies on ternary palladates $CdPd_3O_4$ and $TlPd_3O_4$ using various functionals reveal that $CdPd_3O_4$ is metallic, while $TlPd_3O_4$ is an indirect band gap semiconductor with potential thermoelectric applications, and both compounds are ductile and exhibit paramagnetic behavior [25]. Similarly, XMg_3O_4 (X = Li, Na, K, Rb) compounds have been identified as ferromagnetic, mechanically stable, and half-metallic, with Curie temperatures ranging from 113 K to 537 K [26].

To the best of our knowledge, no prior theoretical or experimental studies have been reported for the Mg_3BaO_4 and Sr_3CdO_4 compounds in the existing literature. Therefore, in this work, we undertake a comprehensive first-principles investigation of these materials. Our study covers a wide range of properties, including structural, mechanical, electronic, and optical properties.

2 Computational details

To investigate the electronic properties of Mg_3BaO_4 and Sr_3CdO_4, we employed the full potential linearized augmented plane wave (FP-LAPW) method [27] within the WIEN2k all-electron code [28], which solves the Kohn-Sham equations [29] at the density functional theory (DFT) level. For structural optimization, we used the Perdew-Burke-Ernzerhof (PBE) functional within the generalized gradient approximation (GGA) to treat the exchange-correlation (XC) energy [30]. In the GGA scheme, the exchange-correlation energy is assumed to be a functional of the spatial gradients and charge density $\rho(r)$, expressed as

$$E_{\mathrm{xc}}^{\mathrm{GGA}} = \int \varepsilon_{\mathrm{xc}} F(\rho, \nabla\rho)\, \mathrm{d}^3 r. \tag{1}$$

To enhance the accuracy of electronic and optical properties, the modified Becke-Johnson (mBJ) potential [31] was utilized, known for its superior performance in estimating band gaps in complex oxides. The mBJ potential is expressed as [32]

$$V_{x,\sigma}^{mBJ}(r) = cV_{x,\sigma}^{BR}(r) + (3c-2)\frac{1}{\pi}\sqrt{\frac{5}{12}}\sqrt{\frac{2t_\sigma(r)}{\rho_\sigma(r)}} \tag{2}$$

where $\rho_\sigma = \sum_{i=1}^{N_\sigma} |\Psi_{i,\sigma}|^2$ represents the electron density, $t_\sigma = \frac{1}{2}\sum_{i=1}^{N_\sigma} \nabla\Psi_{i,\sigma}^* \nabla\Psi_{i,\sigma}$ denotes the kinetic energy of the crystal system, and $V_{x,\sigma}^{BR}$ is the Becke-Roussel (BR) potential [33]. In the FP-LAPW method, the unit cell is divided into two distinct regions: non-overlapping spheres centered at

Table 1: The lattice parameter (a), the bulk modulus (B) and its first pressure derivative (B'), equilibrium volume (V_0) and energy (E_0), formation energy (E_f), cohesive energy (E_{coh}) of Mg_3BaO_4 and Sr_3CdO_4

Compound	a (Å)	B (GPa)	B′	V_0 (a.u.^{3})	E_0 (eV)	E_f (eV/atom)	E_{coh} (eV/atom)
Mg_3BaO_4	4.8241	103.4508	4.3997	757.6077	-246037.65668	-2.834	-5.294
Sr_3CdO_4	5.1018	89.6249	4.4656	896.1268	-420062.01189	-3.163	-5.538
Mg_3CdO_4 [23]	4.445	142.262	4.496	-	-	-5.250	-5.118

atomic positions with a radius R_{MT}, and the interstitial region [34]. In the interstitial region, the potential is expanded using plane wave orbitals, while in the muffin-tin region, the basis set is constructed from spherical harmonics, resembling atomic orbitals. The potential in this approach is expressed as [35]

$$V(r) = \begin{cases} \sum_{lm} V_{lm}(r) Y_{lm}(r), & \text{(Muffin-tin region)}, \\ \sum_{k} V_k e^{ikr}, & \text{(Interstitial region)} \end{cases} \tag{3}$$

In our calculations, a Muffin-tin radius to wave-vector cut-off ratio of $R_{\mathrm{MT}} \times K_{\max} = 7$ was employed. The maximum angular momentum quantum number ($L_{\max}$) was set to 10, and the maximum magnitude of the reciprocal lattice vectors ($G_{\max}$) was set to 12. A $12 \times 12 \times 12$ k-mesh, corresponding to 2000 k-points, was used to ensure convergence, with energy and charge stability thresholds of 10^{-7} Ry and 10^{-5} e, respectively. For the calculation of optical properties, a denser k-mesh of $46 \times 46 \times 46$, comprising 100000 k-points in the full Brillouin zone, was utilized.

3 Results and discussion

3.1 Structural property

Both Mg_3BaO_4 and Sr_3CdO_4 compounds crystallize in a cubic structure belonging to the space group $Pm\bar{3}m$ (No. 221), as shown in Figure 1. In these structures, the Mg/Sr atoms are positioned at the 3c Wyckoff site (0, 1/2, 1/2), while the Ba/Cd atoms occupy the 1a Wyckoff site (0, 0, 0). The O atoms are located at two distinct Wyckoff sites: 3d (0, 0, 1/2) and 1b (1/2, 1/2, 1/2). These specific atomic positions define the crystallographic framework of both materials and play a crucial role in determining their unique physical properties. In order to determine the theoretical lattice constant and ground state energy, Energy-volume optimizations were conducted using Murnaghan's equation of state [36]

$$E_t = E_0 + \frac{VB}{B'(B'-1)} \left[\left(\frac{V_0}{V} \right)^{B'} + B \left(1 - \frac{V_0}{V} \right) - 1 \right] \tag{4}$$

where E_0, V_0, $B = -V\frac{\partial P}{\partial V}$, and $B' = \frac{\partial B}{\partial P}$ are the minimum energy, equilibrium volume, bulk modulus, and the pressure derivative of the bulk modulus, respectively. This approach allowed us to calculate the equilibrium lattice parameter and corresponding energy. For this, we carried out ferromagnetic (FM) and non-magnetic (NM) calculations using the ideal cubic structure. From the calculations, we observed that NM state has lowest energy than FM state which indicates that these compunds are NM in nature.

Furthermore, to check the thermodynamic and chemical stabilities of these compounds, formation (E_f) and cohesive (E_{coh}) energies are computed using the following equations

$$E_f = \frac{E^{total}_{A_3BO_4} - (3E^{bulk}_A + E^{bulk}_B + 4E^{bulk}_{O_4})}{8} \tag{5}$$

$$E_{coh} = \frac{E^{total}_{A_3BO_4} - (3E^{iso}_A + E^{iso}_B + 4E^{iso}_{O_4})}{8} \tag{6}$$

where, A=Mg/Sr, B=Ba/Cd, and O atoms. Calculated lattice parameters (in Å), bulk moduli (B) (in GPa), their pressure derivative (B'), formation (E_f) and cohesive (E_{coh}) energies (in eV/atom) of the structural and ground phase (NM) for Mg_3BaO_4 and Sr_3CdO_4 are detailed in Table 1. The calculated values of lattice parameters are 4.8241 and 5.1018 Å for Mg_3BaO_4 and Sr_3CdO_4, respectively. The lattice parameter for Mg_3BaO_4 of the work is comparable with that of Mg_3CdO_4 [23]. The negative values for both formation and cohesive energies suggest that these compounds are thermodynamically and chemically stable in their NM phase, indicating that they can be successfully synthesized, Figure 2(a,b).

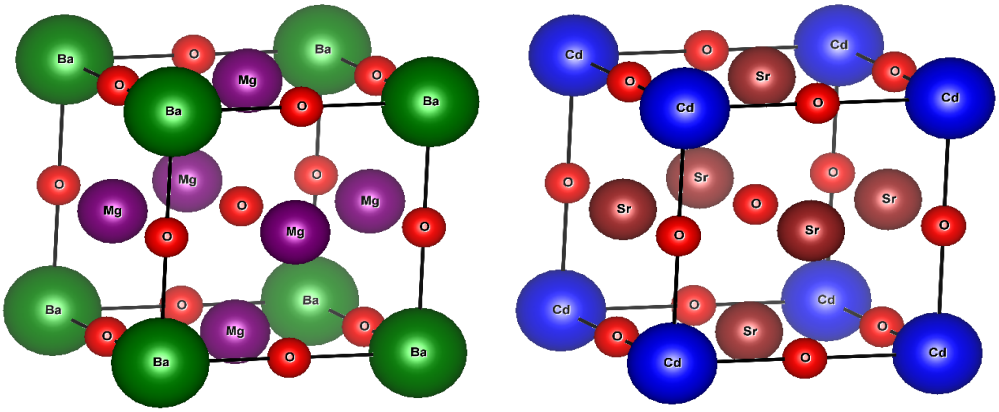

Figure 1: Crystal structure of Mg_3BaO_4 (left) and Sr_3CdO_4 (right).

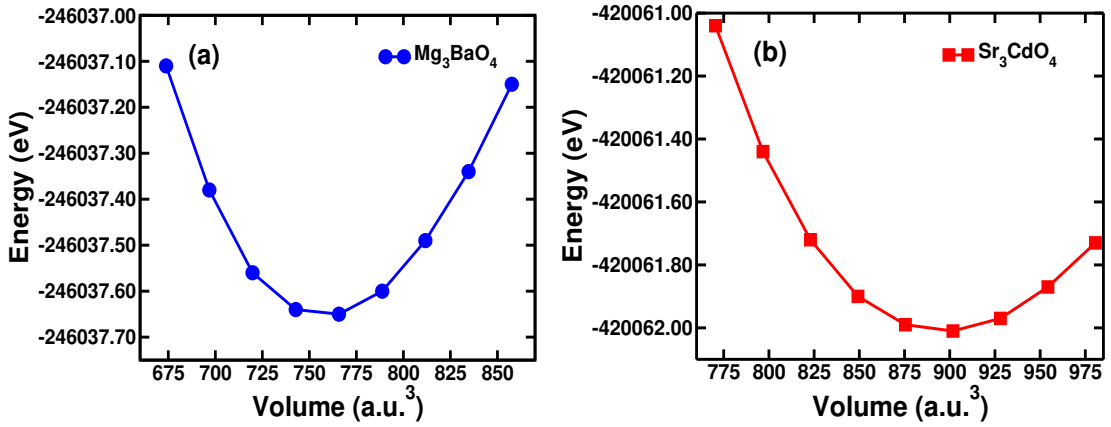

Figure 2: Total energy as a function of volume for (a) Mg_3BaO_4 and (b) Sr_3CdO_4.

3.2 Elastic properties

The elastic properties of materials provide insight into their stability and stiffness. In cubic crystal structures, three independent elastic constants, namely C_{11}, C_{12}, and C_{44}, primarily determine mechanical stability. For mechanical stability these elastic constans must satisfy the Born-Huang (BH) criteria [37], expressed as

$$C_{11}, C_{44} > 0; \quad C_{11} > |C_{12}|; \quad C_{12} < B < C_{11}$$
$$C_{11} - C_{12} > 0; \quad C_{11} + 2C_{12} > 0 \tag{7}$$

The present calculations that both Mg_3BaO_4 and Sr_3CdO_4 compounds are mechanically stable and physically realistic, Table 2. This indicates that these materials respond predictably to applied stress without mechanical instabilities or unrealistic deformation. In other words, their internal structures remain resilient and stable under typical conditions, Figure 3(a). The elastic constants were further employed to calculate key mechanical properties, including the bulk modulus (B), shear modulus (G), Pugh's ratio (B/G), Poisson's ratio (ν), Young's modulus (E), and anisotropy factor (A), using standard expressions [38–40], given below

$$B = \frac{C_{11} + 2C_{12}}{3} \tag{8}$$

$$G = \frac{C_{11} - C_{12}}{2} \tag{9}$$

$$E = \frac{9BG}{3B + G} \tag{10}$$

$$\nu = \frac{3B - 2G}{2(3B + G)} \tag{11}$$

$$A = \frac{2C_{44}}{(C_{11} - C_{12})} \tag{12}$$

The bulk modulus reflects a material's resistance to uniform compression, quantifying its ability to withstand volume changes under applied pressure. A higher bulk modulus signifies greater resistance to deformation. For Mg_3BaO_4 and Sr_3CdO_4, the computed bulk moduli are 103.499 GPa and 97.373 GPa, respectively (Figure 3(b)). These values indicate that Mg_3BaO_4 is more resistant to compression compared to Sr_3CdO_4, highlighting its relative structural robustness. The shear modulus measures resistance to shape changes under parallel forces,

such as twisting or shearing. Higher shear modulus values indicate greater rigidity. For Mg_3BaO_4 and Sr_3CdO_4, the shear moduli are calculated to be 65.606 GPa and 62.615 GPa, respectively, suggesting that Mg_3BaO_4 is more resistant to shearing forces than Sr_3CdO_4. Young's modulus (E), also known as the elastic modulus, quantifies a material's stiffness, describing how it deforms under stress. Its higher value indicates greater rigidity and reduced deformation under applied forces. The Young's modulus values for Mg_3BaO_4 and Sr_3CdO_4 are 162.487 and 154.689 GPa, respectively, confirming that Mg_3BaO_4 is significantly stiffer than Sr_3CdO_4. This increased rigidity can be attributed to stronger bonding interactions and potentially higher lattice rigidity in Mg_3BaO_4, making it less prone to shape changes under mechanical forces. Pugh's ratio (B/G) is used to assess a material's ductility or brittleness. A B/G ratio below

Table 2: The calculated elastic constants C_{ij}, bulk modulus B, shear modulus G, Young's modulus E, Poisson's ratio (ν), Pugh's ratio (B/G), Cauchy pressure ($C_P = C_{12} - C_{44}$), Anisotropy factor (A), transverse sound velocity (v_t), longitudinal sound velocity (v_l), average sound velocity (v_m), Debye temperature (Θ_D), and melting temperature (T_m) of Mg_3BaO_4 and Sr_3CdO_4

Material property	**Mg_3BaO_4**	**Sr_3CdO_4**	**Mg_3CdO_4 [23]**
C_{11} (GPa)	180.034	186.037	248.844
C_{12} (GPa)	65.232	53.041	111.838
C_{44} (GPa)	71.727	60.153	102.618
B (GPa)	103.499	97.373	-
G (GPa)	65.606	62.615	87.272
E (GPa)	162.487	154.689	220.999
ν	0.238	0.235	0.266
B/G	1.578	1.555	-
C_P (GPa)	-6.495	-7.112	-
A	1.249	0.904	1.498
v_t (m/s)	4021.634	3376.232	-
v_l (m/s)	6861.467	5738.034	-
v_m (m/s)	4458.751	3741.865	-
Θ_D (K)	550.353	436.725	-
T_m (K)	1617.000 ± 300	1652.478 ± 300	-

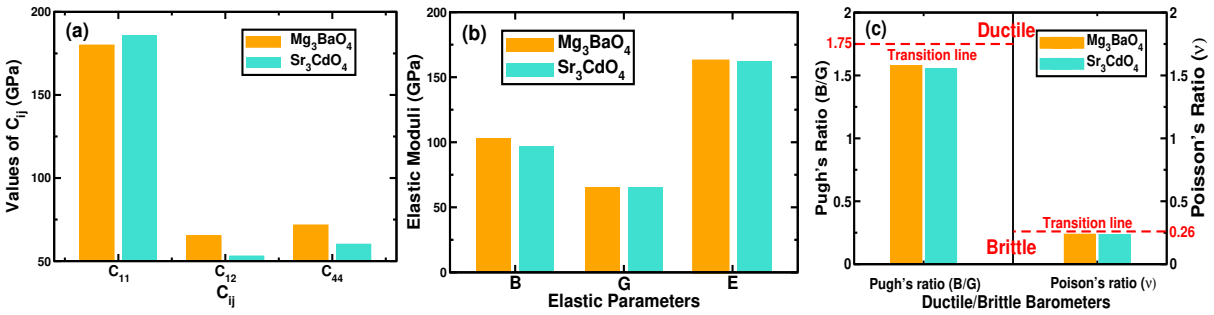

Figure 3: The calculated (a) elastic constants and (b) elastic Moduli (c) ductile/brittle barometers of Mg_3BaO_4 and Sr_3CdO_4.

1.75 indicates brittleness, while a value above 1.75 suggests ductility [41]. For Mg_3BaO_4 and Sr_3CdO_4, the calculated B/G ratios are 1.57 and 1.55, respectively, classifying both materials as brittle (Figure 3(c)). Poisson's ratio (ν) provides additional insight into ductility and brittleness. Generally, a Poisson's ratio below 0.26 suggests brittleness, whereas a value exceeding 0.26 indicates ductility [42]. Both Mg_3BaO_4 and Sr_3CdO_4 exhibit Poisson's ratios of 0.23, corroborating their classification as brittle ma-

terials. These findings imply that both materials are prone to fracture under stress, with limited capacity for plastic deformation.

The Cauchy pressure (C_p), defined as $C_P = C_{12} - C_{44}$, offers insights into the bonding nature of a crystal, distinguishing between ionic and covalent characteristics [43, 44]. Negative C_p values suggest a predominance of covalent bonding, Table 2. For Mg_3BaO_4 and Sr_3CdO_4, the calculated C_p values are -6.495 and -7.112 GPa, respectively, highlighting their covalent bonding nature. The anisotropy factor (A) quantifies the directional dependence of a material's properties. A value of A = 1 indicates isotropy, while deviations from this value signify anisotropic behavior [45, 46]. The computed anisotropy factors for Mg_3BaO_4 and Sr_3CdO_4 are 1.249 and 0.904, respectively, revealing that both materials exhibit anisotropic properties.

The transverse sound velocity (v_t) and longitudinal sound velocity (v_l) are calculated based on their shear modulus (G) and bulk modulus (B) [47, 48], expressed as

$$v_t = \left(\frac{G}{\rho}\right)^{1/2} \tag{13}$$

$$v_l = \left(\frac{3B + 4G}{3\rho}\right)^{1/2} \tag{14}$$

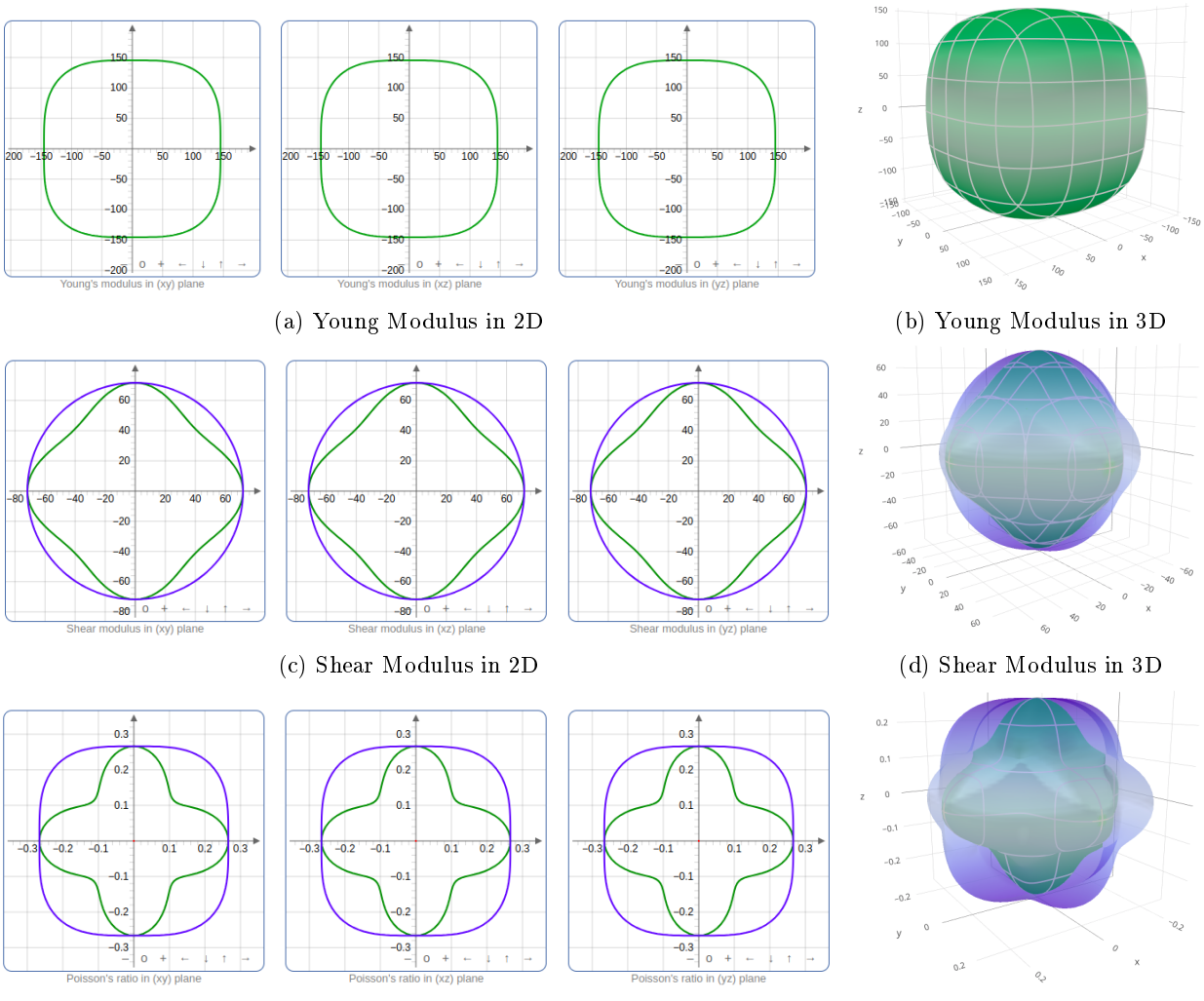

(a) Young Modulus in 2D (b) Young Modulus in 3D

(c) Shear Modulus in 2D (d) Shear Modulus in 3D

(e) Poison's ratio in 2D (f) Poison's ratio in 3D

Figure 4: The left panel show the 2D illustration of variations in Young's modulus, shear modulus and Poisson's ratio of Mg_3BaO_4 and 3D depictions of these parameters are given in the right panel of this graph.

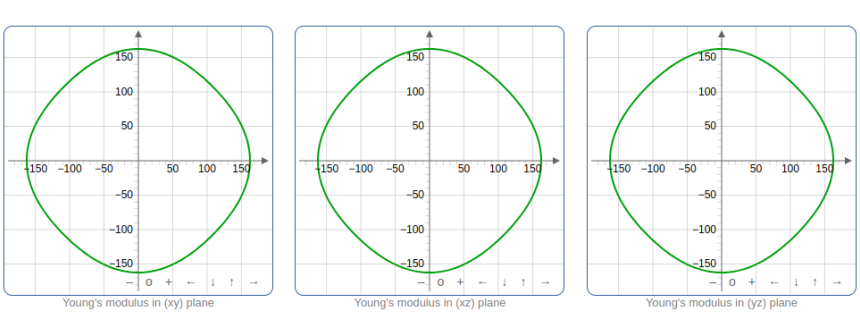

(a) Young Modulus in 2D

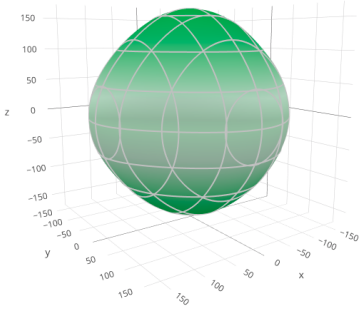

(b) Young Modulus in 3D

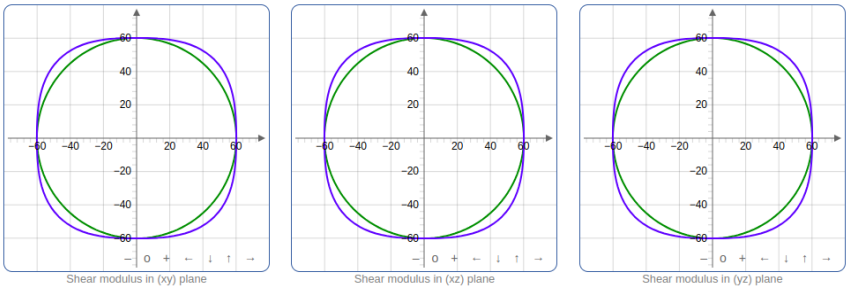

(c) Shear Modulus in 2D

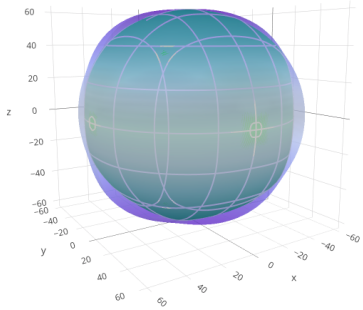

(d) Shear Modulus in 3D

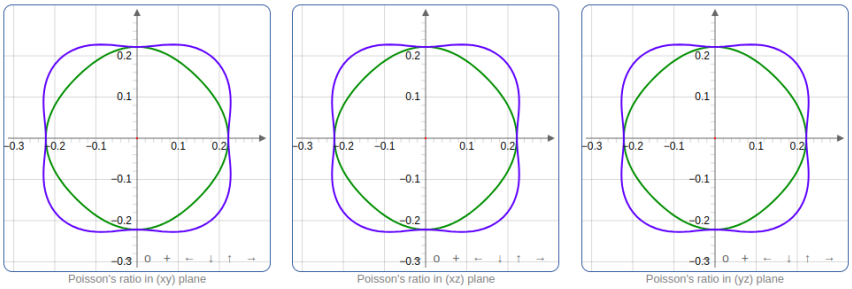

(e) Poison's ratio in 2D

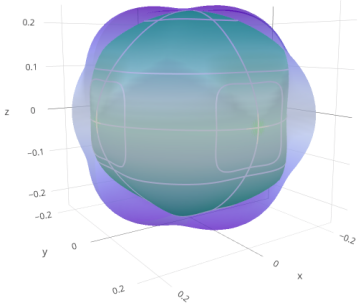

(f) Poison's ratio in 3D

Figure 5: The left panel show the 2D illustration of variations in Young's modulus, shear modulus and Poisson's ratio of Sr_3CdO_4 and 3D depictions of these parameters are given in the right panel of this graph.

where ρ is the density of the compounds. Additionally, the mean sound velocity (v_m) is determined using the relation

$$V_m = \left[\frac{1}{3}\left(\frac{2}{V_t^3} + \frac{1}{V_l^3}\right)\right]^{-1/3} \tag{15}$$

These sound velocities are crucial for understanding the material's elastic behavior. Moreover, the Debye temperature (θ_D), which offers insights into the thermal properties of the crystals, is derived from the Debye model [49]

$$\theta_D = \frac{h}{k_B}\left[\frac{3n}{4\pi} \times \frac{N_A\rho}{M}\right]^{1/3} \times V_m \tag{16}$$

Here, h is Planck's constant, k_B is the Boltzmann constant, N_A is Avogadro's constant, M is the molecular mass, and n represents the number of atoms in the compound. The computed transverse, longitudinal, and mean sound velocities for Mg_3BaO_4 are 4021.634, 6861.467, and 4458.751 m/s, respectively, while for Sr_3CdO_4, they are 3376.232, 5738.034, and 3741.865 m/s, respectively. The corresponding Debye temperatures are calculated to be 550.353 K for Mg_3BaO_4 and 436.725 K for Sr_3CdO_4, reflecting the distinct thermal properties of these materials. These results provide valuable insights into the elastic and thermal behavior of these compounds.

Further, the ELATE code [50] is utilized to generate 2D and 3D visualizations of Young's modulus, shear modulus, and Poisson's ratio of the compounds. These graphical representations provide a deeper understanding of the mechanical behavior by illustrating how these parameters vary across

different planes. The results for Mg_3BaO_4 are presented in Figure 4(a-f), while the corresponding visualizations for Sr_3CdO_4 are shown in Figure 5(a-f). It can be observed that both compounds show anisotropic properties with respect to these elastic moduli, validating the previous findings.

3.3 Electronic properties:

The band gap is a critical property that significantly influences a material's suitability for optical device applications. To investigate the electronic properties of the studied compounds, as illustrated in Figure 6(a-d), we calculated the band structures of Mg_3BaO_4 and Sr_3CdO_4 using the PBE-GGA and TB-mBJ exchange-correlation potentials. Using the PBE-GGA approach, the electronic band gap calculations revealed a direct band gap (Γ-Γ) of 0.79 eV for Mg_3BaO_4 and an indirect band gap (M-Γ) of 0.55 eV for Sr_3CdO_4. However, it is well-known that the PBE-GGA method often underestimates the energy band gaps of materials, which limits its accuracy for quantitative predictions. This limitation is evident in the results for the studied compounds.

To overcome this challenge, we employed the Tran-Blaha modified Becke-Johnson (TB-mBJ) potential, which is widely recognized for its improved accuracy in predicting electronic band gaps. The TB-mBJ calculations provided a direct band gap of 2.29 eV for Mg_3BaO_4 and an indirect band gap of 2.64 eV for Sr_3CdO_4. These results highlight the reliability of the TB-mBJ approach in yielding more precise electronic properties, which are critical for understanding the material's potential applications. In previous studies, Mg_3ZnO_4 was reported to exhibit an indirect band gap of 5.19 eV [22], Figure 6(b,d). Similarly, research on Mg_3CdO_4 identified an indirect band gap of 3.12 eV [23]. The increase in the band gap of Sr_3CdO_4 compared to Mg_3BaO_4 can be attributed to several factors, including its larger lattice constant, which reduces orbital overlap and enhances the band gap, as well as the higher cation polarizability of Sr and Cd, which modifies the effective potential experienced by electrons. Additionally, the more localized Cd-d states compared to Mg-s states further contribute to the separation between the valence and conduction bands, increasing the band gap in Sr_3CdO_4. The distinctive electronic band gap characteristics of these materials hold significant promise for applications in energy storage and the semiconductor industry. However, the absence of both theoretical predictions and experimental data on their band gaps presents a compelling opportunity for further investigation. This study provides a foundational basis for future research, paving the way for a deeper understanding and potential advancements in these compounds.

To gain a deeper understanding of the electronic properties of Mg_3BaO_4 and Sr_3CdO_4, we analyzed their total density of states (TDOS) and partial density of states (PDOS). The results are presented in Figure 7(a-d). The energy range considered for all density of states (DOS) plots extends from -7 to 7 eV. Within this range, the interval referred to as region 1, ranging from -7 to 0 eV, corresponds to the valence band. The Fermi level (E_F) is represented by a dashed line at 0 eV. Additionally, the interval labeled as region 3, extending from 0 to 7 eV, corresponds to the conduction band. In the valence band of Mg_3BaO_4, the primary contributions arise from the O1-p, O2-p, and Ba-s states, with a minor contribution from the Mg-s state. Conversely, in the conduction band, significant contributions originate from the O1-p, O2-p, and Mg-s states, while the Ba-s state plays a minor role. Similarly, for Sr_3CdO_4, the valence band is predominantly influenced by the O1-p, O2-p, and Cd-d states, with a smaller contribution from the Sr-s state. In contrast, the conduction band is characterized by a notable contribution from the O1-p, and O2-p states, with minor contributions from the Sr-s, and Cd-d states. These observations highlight the distinct roles of atomic orbitals in shaping the electronic structure of Mg_3BaO_4 and Sr_3CdO_4.

3.4 Optical properties

The optical properties of Mg_3BaO_4 and Sr_3CdO_4 are crucial for their potential applications in solar cells and other optoelectronic devices. The optical behavior of any material is intrinsically linked to its band gap. To thoroughly investigate these properties, we employed the TB-mBJ potential.

A fundamental aspect of optical analysis is the dielectric constant, $\varepsilon(\omega)$, which describes a material's response to an external electromagnetic field. This dielectric function has both real and imaginary components, expressed as:

$$\varepsilon(\omega) = \varepsilon_1(\omega) + i\varepsilon_2(\omega) \tag{17}$$

where $\varepsilon_1(\omega)$ and $\varepsilon_2(\omega)$ are the real and imaginary components of the complex dielectric function, respectively, and ω represents the angular frequency of the incident photon. The real and imaginary parts of the dielectric function are related by the Kramers-Kronig relations [51, 52], which are given by

$$\varepsilon_1(\omega) = 1 + \frac{1}{\pi}\int_0^\infty \frac{\omega'\varepsilon_2(\omega)}{\omega'^2 - \omega^2} d\omega' \tag{18}$$

$$\varepsilon_1(\omega) = \frac{-2\omega}{\pi} P\int_0^\infty \frac{\varepsilon_1(\omega') - 1}{\omega'^2 - \omega^2} d\omega' \tag{19}$$

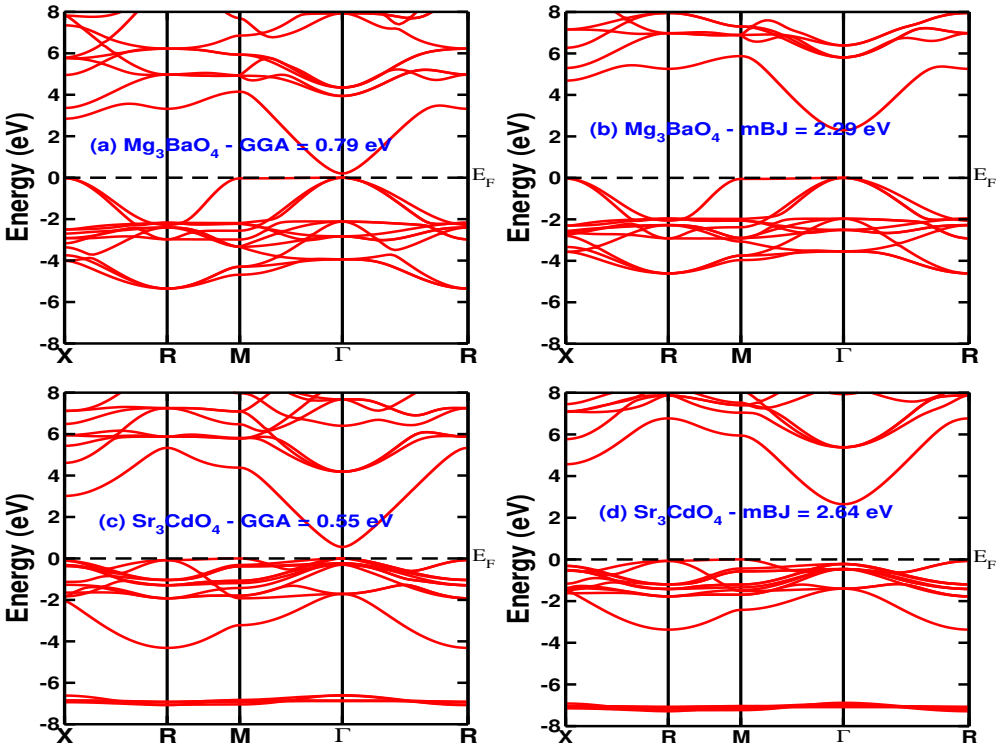

Figure 6: Electronic Band Structure Calculations of Mg_3BaO_4 and Sr_3CdO_4 using PBE-GGA and PBE + TB-mBJ.

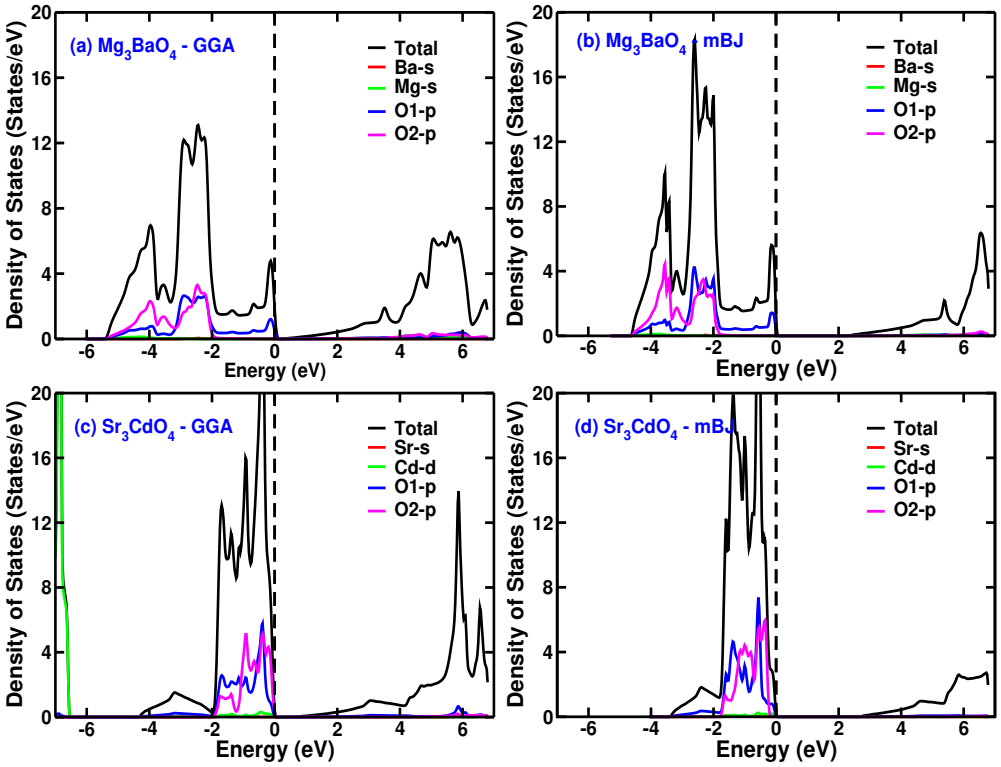

Figure 7: Calculated total and partial density of states of Mg_3BaO_4 and Sr_3CdO_4 using PBE-GGA and PBE + TB-mBJ.

Furthermore, all other optical properties, including the absorption coefficient $\alpha(\omega)$, extinction coefficient $k(\omega)$, refractive index $n(\omega)$, reflectivity $R(\omega)$, conductivity $\sigma(\omega)$, and loss function $L(\omega)$, are determined using the dielectric function, as follows [53, 54]:

$$\alpha(\omega) = \sqrt{2}\omega \left[\sqrt{\varepsilon_1^2(\omega) + \varepsilon_2^2(\omega)} - \varepsilon_1(\omega)\right]^{\frac{1}{2}} \quad (20)$$

$$K(\omega) = \frac{1}{\sqrt{2}} \left[\sqrt{\varepsilon_1^2(\omega) + \varepsilon_2^2(\omega)} - \varepsilon_1(\omega)\right]^{\frac{1}{2}} \quad (21)$$

$$n(\omega) = \frac{1}{\sqrt{2}} \left[\sqrt{\varepsilon_1^2(\omega) + \varepsilon_2^2(\omega)} + \varepsilon_1(\omega)\right]^{\frac{1}{2}} \quad (22)$$

$$R(\omega) = \left|\frac{\sqrt{\varepsilon_1^2(\omega) + \varepsilon_2^2(\omega)} - 1}{\sqrt{\varepsilon_1^2(\omega) + \varepsilon_2^2(\omega)} + 1}\right|^2 \quad (23)$$

$$\sigma(\omega) = \frac{\omega\varepsilon_2}{4\pi} \quad (24)$$

and,

$$L(\omega) = \frac{\varepsilon_1(\omega)}{\varepsilon_1^2(\omega) + \varepsilon_2^2(\omega)} \quad (25)$$

The real part of the dielectric function, $\varepsilon_1(\omega)$, describes the dispersive or polarizing behavior of a material when interacting with light, while the imaginary part, $\varepsilon_2(\omega)$, relates to light absorption.

At static frequency ($\varepsilon_1(0)$), Mg_3BaO_4 exhibits a dielectric constant of 2.91, while Sr_3CdO_4 has a slightly lower value of 2.84, Table 3. These values set the baseline for the material's optical responses. With increasing photon energy, the real part of the dielectric function $\varepsilon_1(\omega)$ peaks at 4.77 for Mg_3BaO_4 at 8.61 eV and at 3.73 for Sr_3CdO_4 at 4.14 eV, as shown in Figure 8(a). Beyond 11.22 eV, $\varepsilon_1(\omega)$ becomes negative for both materials, indicating a transition to metallic behavior [55, 56].

The band gap and the static dielectric function are interconnected through Penn's model [57], which is expressed as

$$\varepsilon_1(\omega) = 1 + \left(\frac{\hbar\omega_p}{E_g}\right)^2 \quad (26)$$

where E_g represents the optical band gap and $\hbar\omega_p$ is the plasma energy. It was found that the static dielectric function value and the maximum of $\varepsilon_1(\omega)$ were higher for Mg_3BaO_4 compared to Sr_3CdO_4. This behavior is attributed to the lower band gap of Mg_3BaO_4, which aligns with the predictions of Penn's model. Both Mg_3BaO_4 and Sr_3CdO_4 compounds exhibit a wide range of absorption spectra, making them particularly advantageous for diverse optical applications. Notably, high polarization is observed in the UV region.

The imaginary part of the dielectric function, $\varepsilon_2(\omega)$, is zero at 0 eV for both Mg_3BaO_4 and Sr_3CdO_4, indicating no energy dissipation at this threshold, as shown in Figure 8(b). The threshold energy value represents the material's optical band gap edges [58]. The optical bandgap, which is approximately 2.293 eV for Mg_3BaO_4 and 2.653 eV for Sr_3CdO_4. These values are closely aligned with their respective electronic bandgaps of 2.297 eV and 2.648 eV. As photon energy exceeds the threshold, $\varepsilon_2(\omega)$ increases sharply, with Mg_3BaO_4 reaching a peak of 4.86 at 9.21 eV, and Sr_3CdO_4 peaking at 3.91 at 9.53 eV. The sharp peaks in ε_2 correspond to electronic transitions between different energy bands. These transitions mark the onset of optical absorption and the excitation of electrons to higher energy states. As a result, both compounds exhibit significant absorption in the UV region, making them excellent candidates for high-performance optoelectronic devices. Their broad absorption capability is especially useful in technologies such as photovoltaic cells, optical sensors, and light-emitting devices, where efficient light capture across a wide spectrum is essential.

The absorption coefficient, $\alpha(\omega)$, is another important parameter that measures the amount of optical energy absorbed by a material per unit length [59]. Figure 8(c) presents the absorption coefficients, measured in units of $10^4\,cm^{-1}$, as a function of energy within the 0-20 eV range. The pattern of the $\alpha(\omega)$ plot closely follows that of the $\varepsilon_2(\omega)$ plot (see Figure 8(b) for both Mg_3BaO_4 and Sr_3CdO_4. This suggests that $\alpha(\omega)$ is linked to the band structures of both compounds. The absorption spectra show an onset edge at 2.293 eV for Mg_3BaO_4 and 2.653 eV for Sr_3CdO_4. Below these energies, from 0 eV to the onset edge, there is negligible or zero absorption, indicating that the material is transparent to incident light in this range. The maximum $\alpha(\omega)$ peaks occur at 17.15 eV with $\alpha = 218.5 \times 10^4$ cm^{-1} for Mg_3BaO_4, and at 12.20 eV with $\alpha = 140.4 \times 10^4$ cm^{-1} for Sr_3CdO_4. The distinct absorption properties of Mg_3BaO_4 and Sr_3CdO_4, with strong UV absorption and transparency in the visible range, make them ideal candidates for optical applications such as UV photodetectors, sensors, deep-UV LEDs, and laser sources.

The extinction coefficient, $K(\omega)$, which measures the absorption of electromagnetic (EM) radiation in materials, is closely related to the imaginary part of the dielectric function, $\varepsilon_2(\omega)$. For Mg_3BaO_4 and Sr_3CdO_4, the $k(\omega)$ values start from zero at 0 eV.

The maximum $k(\omega)$ values are observed at 9.53 eV (1.29) for Mg_3BaO_4 and at 10.40 eV (1.25) for Sr_3CdO_4 (see Figure 8(d). The $k(\omega)$ spectra exhibit a behavior analogous to that of $\varepsilon_2(\omega)$, as shown in Figure 8(b). The onset edges of the $k(\omega)$ peaks align with those observed in $\varepsilon_2(\omega)$, $\alpha(\omega)$, and $\sigma(\omega)$, reflecting a consistent trend. Furthermore, the fluctuations in $k(\omega)$ closely follow the peaks in $\varepsilon_2(\omega)$, demonstrating their interdependence and reinforcing the connection between these optical properties.

The refractive index, $n(\omega)$, is another optical parameter that characterizes the interaction of light with a material. It relates the velocity of light in a vacuum to its velocity within the material, providing valuable insights into optical behavior and energy absorption capabilities. The calculated refractive indices for Mg_3BaO_4 and Sr_3CdO_4 are presented in Figure 8(e). The static refractive index $n(0)$ is determined to be 1.70 for Mg_3BaO_4 and 1.68 for Sr_3CdO_4. As photon energy increases, the refractive index reaches its peak value of 2.28 at 8.72 eV for Mg_3BaO_4 and 1.99 at 7.57 eV for Sr_3CdO_4, both in the ultraviolet (UV) region. These values are summarized in Table 3. The trend in $n(0)$ closely aligns with the static dielectric constant $\varepsilon_1(\omega)$, highlighting their close correlation. Notably, Mg_3BaO_4 exhibits a higher maximum refractive index than Sr_3CdO_4, reflecting its stronger light absorption capability. Additionally, it is worth mentioning that a refractive index value less than unity would imply that the phase velocity of light in the material exceeds the speed of light in a vacuum, a phenomenon associated with anomalous dispersion.

Reflectivity, $R(\omega)$, is an important optical property that provides insight into the surface characteristics of materials by determining the fraction of incident light reflected from a material's surface. This property is particularly significant for evaluating the potential applications of materials in areas such as coatings, optics, and UV filters, where precise control over light reflection is crucial. The reflectivity spectra for Mg_3BaO_4 and Sr_3CdO_4 are illustrated in Figure 8(f).

Table 3: The calculated electronic band gap E_g (eV) and cut off values of various optical parameters for both Mg_3BaO_4 and Sr_3CdO_4.

Material	Band gap (eV)	Optical Parameters		
	TB-mBJ	ε_1 (0)	n (0)	R (0)
Mg_3BaO_4	2.29	2.91	1.70	6.84%
Sr_3CdO_4	2.64	2.84	1.68	6.53%
Mg_3CdO_4 [23]	3.12	2.65	-	-

At zero photon energy, the reflectivity values are observed to be 6.84% for Mg_3BaO_4 and 6.53% for Sr_3CdO_4, Table 3. As the energy of the incident radiation increases, $R(\omega)$ also rises, with Mg_3BaO_4 exhibiting a pronounced peak of 48.69% at 17.56 eV and Sr_3CdO_4 displaying a peak of 30.50% at 12.80 eV, both situated within the UV region. According to previous theoretical work, Mg_3CdO_4 has been reported to exhibit a maximum reflectivity of around 48% at 19 eV [23]. Notably, within the bandgap energy range, $R(\omega)$ remains minimal, indicating that the compounds are transparent to photon energies below the bandgap. This transparency underscores their potential for applications in optics-related fields, particularly in lens fabrication [58,60,61].

Optical conductivity, $\sigma(\omega)$, is a critical parameter describing how well a material conducts light, determined by transitions between energy bands. It also provides insights into the bond-breaking processes when high-energy electromagnetic waves interact with a material's surface. As shown in Figure 8(g), the optical conductivity of Mg_3BaO_4 and Sr_3CdO_4 follows a pattern similar to their absorptivity (see Figure 8(c)). The conductivity begins to rise when photons with energy above a threshold frequency interact with the material's surface. For Mg_3BaO_4, the optical conductivity reaches a maximum value of 6190.98 Ωcm^{-1} at 16.25 eV, while for Sr_3CdO_4, it peaks at 5067.48 Ωcm^{-1} at 10.29 eV. These high values indicate the materials' efficiency in conducting light at high energies, particularly in the ultraviolet (UV) range. The peaks in optical conductivity are a direct result of interband transitions between valence band states and conduction band states. This highlights the strong interaction of these states with high-energy photons, making these materials suitable for advanced UV optoelectronic applications.

When light traverses a material, interactions between photons and the material's components can lead to energy losses, affecting the photons' ve-

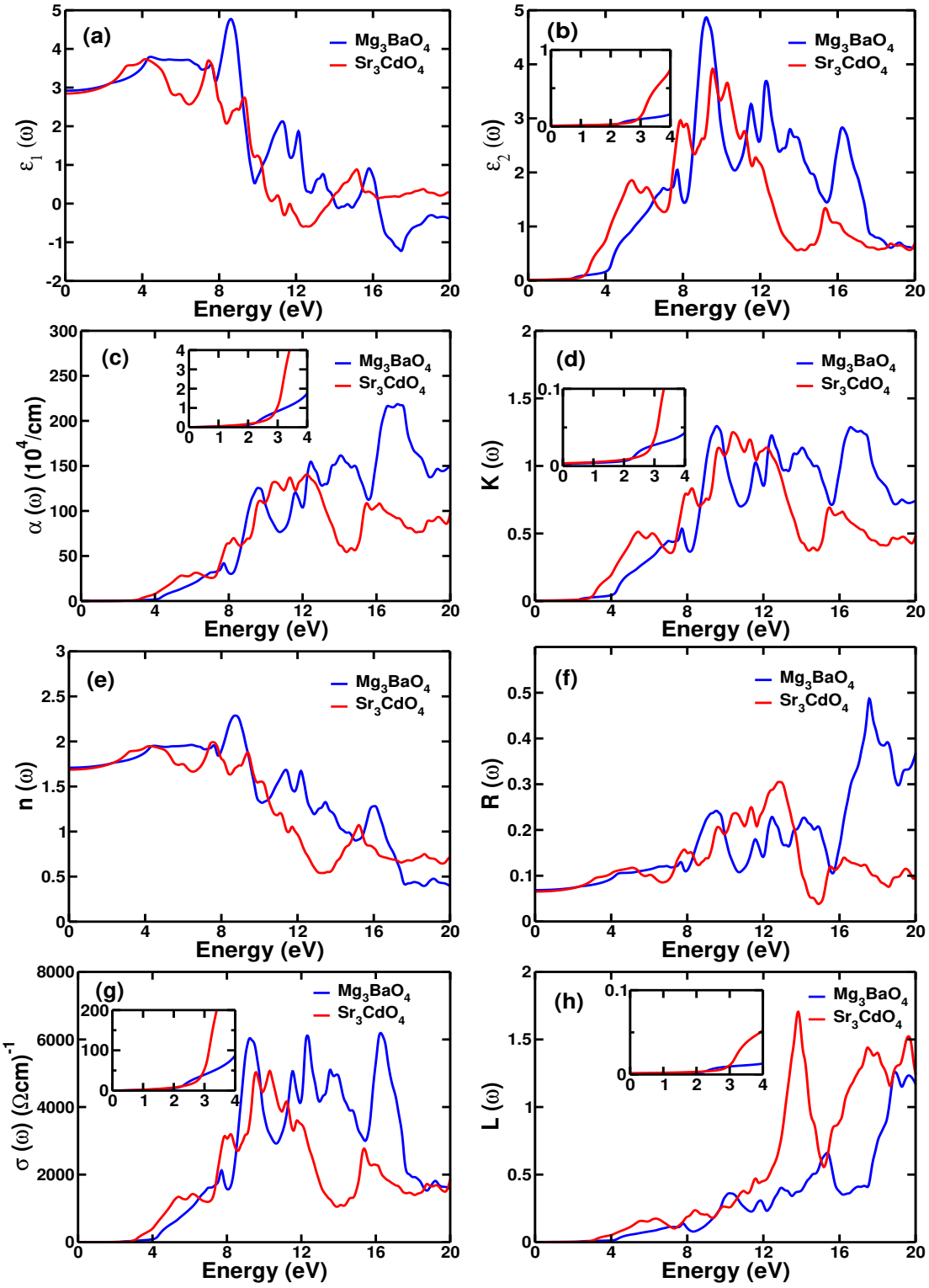

Figure 8: Optical properties of Mg_3BaO_4 and Sr_3CdO_4 including dielectric function, absorption, extinction, refraction, reflectivity, conductivity, and energy loss spectra.

locity. The energy loss function, which reflects these interactions, is analyzed for Mg_3BaO_4 and Sr_3CdO_4 in the energy range of 0-20 eV, as shown in Figure 8(h). For Mg_3BaO_4, the maximum energy loss occurs at 18.92 eV, whereas for Sr_3CdO_4, it is observed at 13.83 eV with higher intensity compared to Mg_3BaO_4. This indicates stronger photon-material interactions in Sr_3CdO_4 at these energies. The present study of the optical properties of Mg_3BaO_4 and Sr_3CdO_4, analyzed in terms of the dielectric function, refractive index, absorption coefficient, reflectivity, and loss function, demon-

strates consistency with previously reported data for Mg_3CdO_4 [23], emphasizing the influence of cationic substitution on their potential optoelectronic applications.

4 Conclusion

In this study, we comprehensively investigated the structural, electronic, and optical properties of Mg_3BaO_4 and Sr_3CdO_4 compounds using first-principles calculations based on density functional theory (DFT). Structural analysis confirmed the thermodynamic and mechanical stability of both materials, indicating their suitability for practical applications. Electronic band structure calculations, using both PBE-GGA and the more accurate TB-mBJ methods. TB-mBJ method, revealed band gaps of 2.29 eV (direct) for Mg_3BaO_4 and 2.64 eV (indirect) for Sr_3CdO_4, highlighting their potential for optoelectronic applications. Optical properties further underscored the suitability of Mg_3BaO_4 and Sr_3CdO_4 for advanced optoelectronic devices. Both materials exhibit strong ultraviolet absorption, with optical band gaps closely aligned with their electronic counterparts. The calculated dielectric functions, refractive indices, and absorption coefficients suggest their applicability in solar cells, optical sensors, and light-emitting devices. Moreover, their exceptional UV absorption, transparency in the visible spectrum, and favorable refractive indices make them ideal candidates for developing UV photodetectors and photovoltaic devices. Their broad absorption range facilitates efficient energy harvesting across both ultraviolet and visible spectra, while their low reflectivity and high extinction coefficients suggest significant potential for use in anti-reflective coatings and laser-based technologies. These findings position Mg_3BaO_4 and Sr_3CdO_4 as promising candidates for next-generation optoelectronic technologies.

Conflict of interest

The authors of the work declare that there is no known or unknown potential conflict of interest.

Authors' contributions

UC: Formal analysis, methodology, data validation, data curation, software and writing first draft. SD: Methodology, data visualization, software and formal analysis. GCP: Data curation and validation. SKY: Resources, supervision and editing the manuscript.

References

[1] Park DS, Rata AD, Dahm RT, Chu K, Gan Y, Maznichenko I, et al. Controlled Electronic and Magnetic Landscape in Self-Assembled Complex Oxide Heterostructures. Advanced Materials. 2023;35(32):2300200.

[2] Rata AD, Herrero-Martin J, Maznichenko IV, Chiabrera FM, Dahm RT, Ostanin S, et al. Defect-induced magnetism in homoepitaxial SrTiO3. APL materials. 2022;10(9).

[3] Muscas G, Prabahar K, Congiu F, Datt G, Sarkar T. Nanostructure-driven complex magnetic behavior of Sm2CoMnO6 double perovskite. Journal of Alloys and Compounds. 2022;906:164385.

[4] Jin L, Su X, Shi J, Shih KC, Cintron D, Cai T, et al. Crystalline mesoporous complex oxides: porosity-controlled electromagnetic response. Advanced Functional Materials. 2020;30(15):1909491.

[5] Trier F, Noël P, Kim JV, Attané JP, Vila L, Bibes M. Oxide spin-orbitronics: spin–charge interconversion and topological spin textures. Nature Reviews Materials. 2022;7(4):258-74.

[6] Ramesh R, Martin L. Electric field control of magnetism: multiferroics and magnetoelectrics. La Rivista del Nuovo Cimento. 2021;44(5):251-89.

[7] Longo C, T Galante M, Fitzmorris R, Zhang JZ, Taylor SFR, Mohapatra J, et al. Complex oxides based on silver, bismuth, and tungsten: syntheses, characterization, and photoelectrochemical behavior. The Journal of Physical Chemistry C. 2018;122(25):13473-80.

[8] Lorenz M, Rao MR, Venkatesan T, Fortunato E, Barquinha P, Branquinho R, et al. The 2016 oxide electronic materials and oxide interfaces roadmap. Journal of Physics D: Applied Physics. 2016;49(43):433001.

[9] Lee S, Apgar BA, Martin LW. Strong Visible-Light Absorption and Hot-Carrier Injection in TiO2/SrRuO3 Heterostructures. Advanced Energy Materials. 2013;3(8):1084-90.

[10] Sha R, Basak A, Maity PC, Badhulika S. ZnO nano-structured based devices for chemical and optical sensing applications. Sensors and Actuators Reports. 2022;4:100098.

[11] Goel R, Jha R, Ravikant C. Investigating the structural, electrochemical, and optical properties of p-type spherical nickel oxide (NiO) nanoparticles. Journal of Physics and Chemistry of Solids. 2020;144:109488.

[12] Geldasa FT, Kebede MA, Shura MW, Hone FG. Experimental and computational study of metal oxide nanoparticles for the photocatalytic degradation of organic pollutants: a review. RSC advances. 2023;13(27):18404-42.

[13] Zhang K, Han X, Hu Z, Zhang X, Tao Z, Chen J. Nanostructured Mn-based oxides for electrochemical energy storage and conversion. Chemical Society Reviews. 2015;44(3):699-728.

[14] Yoon J, Kim KS, Hong WK. Thermochromic Vanadium Dioxide Nanostructures for Smart Windows and Radiative Cooling. Chemistry–A European Journal. 2024:e202400826.

[15] Tingting S, Fuchun Z, Weihu Z. Density functional theory study on the electronic structure and optical properties of SnO2. Rare Metal Materials and Engineering. 2015;44(10):2409-14.

[16] Xu G, Li L, Shen Z, Tao Z, Zhang Y, Tian H, et al. Magnetite Fe3O4 nanoparticles and hematite α-Fe2O3 uniform oblique hexagonal microdisks, drum-like particles and spindles and their magnetic properties. Journal of Alloys and Compounds. 2015;629:36-42.

[17] Chevalier S, Bonnet G, Larpin J. Metal-organic chemical vapor deposition of Cr2O3 and Nd2O3 coatings. Oxide growth kinetics and characterization. Applied Surface Science. 2000;167(3-4):125-33.

[18] Ketfi ME, Essaoud SS, Al Azar S, Al-Reyahi AY, Mousa AA, Mufleh A. Insight into the spin-polarized structural, optoelectronic, magnetic, thermodynamic, and thermoelectric properties of PdBO2 (B= Al, Cr, and Rh) Delafossite semiconductor. Optical and Quantum Electronics. 2023;55(11):1013.

[19] Zerarga F, Bouhemadou A, Khenata R, Bin-Omran S. Structural, electronic and optical properties of spinel oxides ZnAl2O4, ZnGa2O4 and ZnIn2O4. Solid State Sciences. 2011;13(8):1638-48.

[20] Allali D, Bouhemadou A, Zerarga F, Sahnoune F. Electronic and optical properties of the spinel oxides GeB2O4 (B= Mg, Zn and Cd): An ab-initio study. Journal of Nanoelectronics and Optoelectronics. 2019;14(7):945-52.

[21] Meng Y, Shi W, Lu C, Yang S, Yang Q, Deng J. First-principles study of structural, elastic, electronic and optical properties of zinc ferrite spinel. In: IOP Conference Series: Materials Science and Engineering. vol. 569. IOP Publishing; 2019. p. 022016.

[22] Zaoui A, Ferhat M. Transforming nonisostructural wurtzite (ZnO) and rocksalt (MgO) II-VI compounds into stable alloy: The case of MgZnO. Superlattices and Microstructures. 2020;145:106623.

[23] Djezzar N, Driss-Khodja K, Amrani B. Exploring dynamical, mechanical and optoelectronic properties of cubic Mg3CdO4: First-principle study. Materials Today Communications. 2021;26:102106.

[24] Keteb M, Boutaleb H, Zemouli M, Khelfaoui F, Amara K, Akil Z, et al. New half-metallic ferromagnetic oxides XBe3O4 (X= Li and Na). Computational Condensed Matter. 2022;31:e00665.

[25] Khan A, Ali Z, Khan I, Ahmad I. First-Principles Study of Electronic Structure, Mechanical, and Thermoelectric Properties of Ternary Palladates CdPd 3 O 4 and TlPd 3 O 4. Journal of Electronic Materials. 2018;47:1871-80.

[26] Nouri T, Khelfaoui F, Benallou Y, Lakhdari H, Amara K, Boutaleb H, et al. Theoretical design of novel half-metallic alloys XMg 3 O 4 (X= Li, Na, K, Rb). Applied Physics A. 2021;127:1-9.

[27] Blaha P, Schwarz K, Sorantin P, Trickey S. Full-potential, linearized augmented plane wave programs for crystalline systems. Computer physics communications. 1990;59(2):399-415.

[28] Blaha P, Schwarz K, Madsen GK, Kvasnicka D, Luitz J, et al. wien2k. An augmented plane wave+ local orbitals program for calculating crystal properties. 2001;60(1).

[29] Kohn W, Sham LJ. Self-consistent equations including exchange and correlation effects. Physical review. 1965;140(4A):A1133.

[30] Perdew JP, Burke K, Ernzerhof M. Generalized gradient approximation made simple. Physical review letters. 1996;77(18):3865.

[31] Becke AD, Johnson ER. A simple effective potential for exchange. The Journal of chemical physics. 2006;124(22).

[32] Tran F, Blaha P. Accurate Band Gaps of Semiconductors and Insulators with a Semilocal Exchange-Correlation Potential. Physical review letters. 2009;102(22):226401.

[33] Becke AD, Roussel MR. Exchange holes in inhomogeneous systems: A coordinate-space model. Physical Review A. 1989;39(8):3761.

[34] Allali D, Bouhemadou A, Bin-Omran S. Theoretical prediction of the structural, electronic and optical properties of SnB2O4 (B= Mg, Zn, Cd). Computational materials science. 2012;51(1):194-205.

[35] Saeed M, Noor Z, Laref A, Althib H, Flemban TH, Murtaza G. Insights into the structural, electronic and optical properties of MgA2B4 (A= Sc, Y; B= S, Se) spinel compounds: direct energy band gap materials. Materials Science in Semiconductor Processing. 2021;127:105736.

[36] Murnaghan FD. The compressibility of media under extreme pressures. Proceedings of the National Academy of Sciences. 1944;30(9):244-7.

[37] Born M, Huang K. Dynamical theory and experiment I. Publishers, Berlin. 1982.

[38] Wang S, Ye H. First-principles study on elastic properties and phase stability of III–V compounds. Physica status solidi (b). 2003;240(1):45-54.

[39] Chaudhary U, Kaphle G, Yadav S. Pressure-dependent structural, elastic, electronic, thermodynamic, and optical properties of LuGaO3 perovskite: A first-principles study. AIP Advances. 2025;15(8).

[40] Dahal S, Chaudhary U, Khatri P, Yadav SK, Adhikari NP. Ab initio study of structural, vibrational, mechanical, electronic and thermoelectric properties of SrAlSiH hydride for energy harvesting applications. Bulletin of Materials Science. 2026;49(3):205.

[41] Pugh S. XCII. Relations between the elastic moduli and the plastic properties of polycrystalline pure metals. The London, Edinburgh, and Dublin Philosophical Magazine and Journal of Science. 1954;45(367):823-43.

[42] Frantsevich IN. Elastic constants and elastic moduli of metals and insulators. Reference book. 1982.

[43] Pettifor D. Theoretical predictions of structure and related properties of intermetallics. Materials science and technology. 1992;8(4):345-9.

[44] Eberhart ME, Jones TE. Cauchy pressure and the generalized bonding model for nonmagnetic bcc transition metals. Physical Review B—Condensed Matter and Materials Physics. 2012;86(13):134106.

[45] Chung D, Buessem W. The elastic anisotropy of crystals. Journal of Applied Physics. 1967;38(5):2010-2.

[46] Kube CM. Elastic anisotropy of crystals. AIP advances. 2016;6(9).

[47] Schreiber E, Anderson OL, Soga N, Bell JF. Elastic constants and their measurement. 1975.

[48] Chaudhary U, Chaudhary S, Yadav DK, Kaphle GC, Yadav SK. First-Principles Investigation of Structural, Elastic, Electronic, and Optical Properties of AcMO3 (M= B, Sc) Perovskites. physica status solidi (b). 2025;262(5):2400574.

[49] Anderson OL. A simplified method for calculating the Debye temperature from elastic constants. Journal of Physics and Chemistry of Solids. 1963;24(7):909-17.

[50] Gaillac R, Pullumbi P, Coudert FX. ELATE: an open-source online application for analysis and visualization of elastic tensors. Journal of Physics: Condensed Matter. 2016;28(27):275201.

[51] Johnson D. A Fourier series method for numerical Kramers-Kronig analysis. Journal of Physics A: Mathematical and General. 1975;8(4):490.

[52] Xiong K, Robertson J, Clark S. Behavior of hydrogen in wide band gap oxides. Journal of Applied Physics. 2007;102(8).

[53] Geleta TA, Behera D, Bouri N, Rivera VJR, Gonzalo FM. First principles insight into the study of the structural, stability, and optoelectronic properties of alkali-based single halide perovskite ZSnCl3 (Z= Na/K) materials for photovoltaic applications. Journal of Computational Chemistry. 2024;45(30):2574-86.

[54] Yadav SK, Dahal S, Chaudhary U, Pokharel P, Adhikari D. Hydrostatic Pressure-Induced Structural, Mechanical, Electronic, Optical, Thermoelectric and Radiation Shielding Properties of RBeO3 (R= Zr, Hf) Perovskites: A Theoretical Study. Journal of Alloys and Compounds Communications. 2026:100222.

[55] Kittel C, McEuen P. Introduction to solid state physics. John Wiley & Sons; 2018.

[56] Delerue C, Allan G, Niquet YM. Collective excitations in charged nanocrystals and in close-packed arrays of charged nanocrystals. Physical Review B—Condensed Matter and Materials Physics. 2005;72(19):195316.

[57] Penn DR. Wave-number-dependent dielectric function of semiconductors. Physical review. 1962;128(5):2093.

[58] Al-Qaisi S, Mushtaq M, Alzahrani JS, Alkhaldi H, Alrowaili Z, Rached H, et al. First-principles

calculations to investigate electronic, structural, optical, and thermoelectric properties of semiconducting double perovskite Ba2YBiO6. Micro and Nanostructures. 2022;170:207397.

[59] Dasgupta PK, Bellamy HS, Liu H, Lopez JL, Loree EL, Morris K, et al. Light emitting diode based flow-through optical absorption detectors. Talanta. 1993;40(1):53-74.

[60] Khan SN, Jehan A, Husain M, Rahman N, Tirth V, Shah SA, et al. Predicting structural, elastic, and optoelectronic properties of oxide perovskites HfXO3 (X= Be, Mg) employing the DFT approach. Optik. 2024;303:171724.

[61] Jehan A, Husain M, Tirth V, Algahtani A, Uzair M, Rahman N, et al. Investigation of the structural, electronic, mechanical, and optical properties of NaXCl 3 (X= Be, Mg) using density functional theory. RSC advances. 2023;13(41):28395-406.